Probing Nanoscale Self-Assembly of Nonfluorescent Small Molecules inside Live Mammalian Cells

Yuan Gao,[†] Cristina Berciu,[‡] Yi Kuang,[†] Junfeng Shi,[†] Daniela Nicastro,[‡] and Bing Xu[†,*]

[†]Department of Chemistry and [‡]Department of Biology, Brandeis University, 415 South Street, Waltham, Massachusetts 02454, United States

ABSTRACT Like cellular proteins that form fibrillar nanostructures, small hydrogelator molecules self-assemble in water to generate molecular nanofibers. In contrast to the well-defined (dys)functions of endogenous protein filaments, the fate of intracellular assembly of small molecules remains largely unknown. Here we demonstrate the imaging of enzyme-triggered self-assembly of nonfluorescent small molecules by doping the molecular assemblies with a fluorescent hydrogelator. The cell fractionation experiments, fluorescent imaging, and electron microscopy indicate that the hydrogelators self-assemble and localize to the endoplasmic reticulum (ER) and are likely processed *via* the cellular secretory pathway (*i.e.*, ER—Golgi—lysosomes/secretion). This work, as the first example of the use of correlative light and electron microscopy for probing the self-assembly of nonfluorescent small molecules inside live mammalian cells, not only establishes a general strategy to provide the spatiotemporal profile of the assemblies of small molecules inside cells but may lead to a new paradigm for regulating cellular functions based on the interactions between the assemblies of small molecules (*e.g.*, molecular nanofibers) and subcellular organelles.

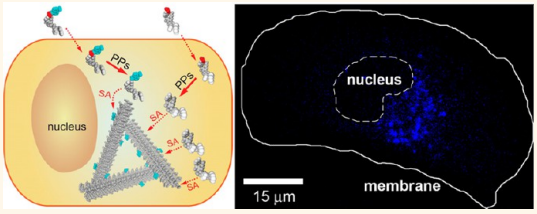

KEYWORDS: self-assembly · small molecule · nanofibers · intracellular · localization · enzyme

INTRODUCTION

Self-assembly of biomacromolecules into fibrillar nanostructures is a fundamental process in both prokaryotic and eukaryotic cells. While the cytoskeletal filaments (*e.g.*, F-actin, lamin, or microtubules) are essential for cell mechanics,[1] the self-assembly of aberrant proteins into nanofibers is closely associated with neurodegenerative diseases, such as Alzheimer's, Pick's, Parkinson's, or Huntington's disease.[2] Due to their importance in cell biology, intracellular protein filaments (normal and abnormal) have attracted intensive research activities on many levels (organismic to molecular). These investigations have provided valuable insights, such as the identification of an array of cytoskeleton-regulatory proteins that are responsible for actin-based cellular phenomena,[3] the elucidation of the noncovalent bonds for interconnecting the fibers in intermediate filaments,[4] and the intracellular protein-degradation pathway for removing abnormal protein filaments.[5] These advances not only contribute significantly to the understanding of the molecular mechanism of intracellular protein filament formation and function but lay the foundation for the study of intracellular nanofibers self-assembled or polymerized from exogenous molecules, which is scientifically intriguing and potentially significant, but has barely been explored.[6,7]

Small-molecular hydrogelators[8,9] that self-assemble in water to form molecular nanofibers[8,10] share common features, such as amphiphilicity and the formation of noncovalent bonds (*e.g.*, hydrogen bonding, hydrophobic interactions, and ionic forces), with the proteins that form the intracellular filaments. Besides being driven by noncovalent bonds to form ordered filamentous assemblies, several features of the hydrogelators make them an attractive system for exploring the properties of molecular nanofibers in cells. First, noncovalent bonds between the hydrogelator molecules promote the interactions among the molecular nanofibers, resulting in their entanglement and the entrapment of water in the nanoscale interstices, a process that is called supramolecular hydrogelation.[8] The macroscopic

* Address correspondence to bxu@brandeis.edu.

Received for review July 17, 2013 and accepted September 18, 2013.

Published online September 25, 2013
10.1021/nn403664n

changes of hydrogelation, *i.e.*, the stoppage of liquid flow, can be easily detected by eye, and thus the formation of a hydrogel serves as a simple assay for rapid screening of a small molecule as a hydrogelator for forming molecular nanofibers. Second, because of their small size, hydrogelators (or their precursors) easily enter cells *via* passive diffusion,[11] which makes it possible to use the cell machinery and fundamental biological processes (*e.g.*, enzyme catalysis) to regulate intracellular self-assembly and the formation of molecular nanofibers. Third, the molecular nanofibers of hydrogelators may exhibit unexpected bioactivities, for example, the self-assembling of small molecules to form molecular nanofibers that promote activation of procaspase-3,[12] disrupt the elongation of microtubules,[13] and serve as a mimic of cytoskeleton in a model protocell.[14]

Our previous study has demonstrated a successful strategy to image real-time molecular self-assembly inside live cells, which occurs in a short time (<1 h) on the endoplasmic reticulum (ER) because the process is predominantly initiated by protein-tyrosine phosphatase 1B (PTP1B) with high activity on the cytoplasmic face of the ER. Furthermore, we are able to identify that the micromorphology of these intracellular molecular assemblies is nanofibers after cell fractionation.[15] Nevertheless, there is a major limitation on the requirement of fluorescence labeling. Actually, fluorescence labeling is the most common technique in the biological analysis[16−18] but has been found to raise certain undesired issues, *e.g.*, toxicity[19] and alteration of macromolecular interactions.[20] Consequently, it usually requires an extensive study to confirm the innocence of the attached fluorophores,[21] or researchers may turn to the label-free imaging technique based on the vibration spectrum of the target molecule, which requires specialized equipment.[22] However, it remains unknown whether the supramolecular self-assembly will induce notable molecular vibration shift for the stimulated Raman scattering (SRS) microscopy to distinguish molecular aggregates from their monomers.

Hence, in this work we manage to image the self-assembly of small molecules without fluorescence labeling (native form) inside mammalian cells with a doping method[23,24] after a longer incubation time (2 days). That is, by incorporating dansyl (DNS)-labeled molecules into the self-assembly of the native molecules, we are able to determine the formation, localization, and progression of molecular assemblies generated from the nonfluorescent small molecular hydrogelators[8,25] by an enzyme-triggered hydrogelation mechanism[25−29] inside live mammalian cells. We confirmed that, upon enzyme catalysis, the precursors of the hydrogelators turn into the corresponding hydrogelators and self-assemble into molecular assemblies. We demonstrated that (i) the precursors passively diffuse inside cells; (ii) the molecular assemblies occur on ER because the cell fraction containing ER triggers the most rapid sol−gel transformation *in vitro*; and (iii) correlative light and electron microscopy (CLEM)[30] further indicates that the molecular assemblies localize near or inside the ER and are likely processed *via* the cellular secretory pathway (*e.g.*, ER−Golgi−lysosomes/secretion[31]) by cells, albeit less efficiently. This work not only establishes a general strategy to provide the spatiotemporal profile of molecular assemblies inside cells but indicates that molecular assemblies of small molecules may provide a new model system to mimic and to understand the cellular mechanisms and processes related to endogenous-normal and aberrant-protein nanofibers.

RESULTS AND DISCUSSIONS

Figure 1A shows the structures of the nonfluorescent precursor (**1a**) and its fluorescent analogue (**2a**) with DNS labeling, as well as the corresponding dephosphorylated products (**1b**, **2b**) catalyzed by a cellular phosphatase. Critical components of these molecules are a self-assembly motif[32] and an enzyme-cleavable group (here the phosphate ester on a tyrosine residue). Upon catalytic dephosphorylation by an alkaline phosphatase (ALP), **1a** converts to hydrogelator **1b**, which self-assembles in water to form molecular assemblies (11 ± 2 nm in diameters), starting at the critical concentration of 235 μM (0.18 mg/mL) (Figure S1). At a 10-times higher concentration, molecular assemblies of hydrogelator **1b** entangle and generate self-supported hydrogels (Figure 1B).[33]

In a recent *in vitro* study we already demonstrated the hydrogelation and the formation of molecular assemblies by self-assembly of the small molecule **1b** in water.[33] However, here we explore the behavior of this hydrogelator in a cellular environment, which is highly crowded with a variety of cellular organelles and a large amount of biomacromolecules. This high degree of complexity presents a challenge for the direct observation of the molecular assemblies in living cells.[34] While **1a** conjugated with different fluorophores has shown a drastically distinguishable spatiotemporal distribution of molecular aggregates within a cellular environment, the fluorophore-labeled molecules still differ from the native molecules. Because fluorescent microscopy is a highly sensitive technique, we choose to dope a small amount of fluorescent **2b** into the nanofibers of **1b**, which will allow the visualization of the assemblies of **1b** under a fluorescent microscope.

As shown in Figure 1C, being treated with ALP, the precursor **2a** (5.5 mM or 6 mg/mL) transforms into the hydrogelator **2b**, which also self-assembles in water to generate a transparent, fluorescent hydrogel within 2 h. Similar to the enzymatically formed molecular assemblies of **1b**, the molecular assemblies of **2b** are 11 ± 2 nm in diameter and several micrometers in length (Figure 1B and C). Their structural similarity allows

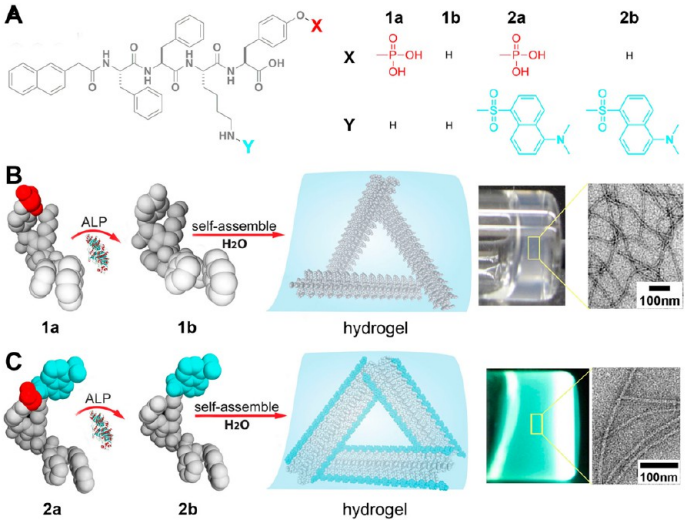

Figure 1. (A) Molecular structures of precursors 1a and 2a and their corresponding hydrogelators 1b and 2b, respectively. (B and C) Illustrations showing the basic steps of enzyme-instructed self-assembly and formation of molecular assemblies and hydrogels: the precursor molecules 1a (B) and 2a (C) are converted to hydrogelators 1b (B) and 2b (C) by dephosphorylation catalyzed by alkaline phosphatase (ALP); these hydrogelators self-assemble in water to form molecular assemblies that generate hydrogels. Toward the right, optical images of hydrogels of the small molecules 1b (B) and 2b (C) (ALP-catalyzed conversion of 1a (0.2 wt %, 2.35 mM) (B), ALP-catalyzed conversion of 2a (0.6 wt %, 5.5 mM) (C)). The zoom-in transmission electron microscope (TEM) images on the very right shows the detailed structure of negatively stained molecular assemblies of 1b (B) and 2b (C).

hydrogelators **1b** and **2b** to coassemble into the same molecular assemblies (Figure S2). This property is useful for cell imaging, because the ratio between the two components can be tuned to optimize fluorescence imaging conditions.

To study whether the nonfluorescent precursor molecules enter and remain in living cells and then transform into mature hydrogelators, we incubated HeLa cells with 500 μM **1a** for 2 days, washed extracellular precursors away, lysed the cells, and then determined the concentration of **1a** and **1b** by LC-MS (Figure 2A, Figure S3A,B). We found that the average concentration of **1b** inside HeLa cells is 0.26−0.94 mg/mL (0.34−1.23 mM), which is above the critical concentration of forming molecular assemblies determined by *in vitro* tests. This result establishes both that intracellular phosphatases convert **1a** to **1b** and that the intracellular accumulation of **1b** is sufficiently high to drive intracellularly the formation of molecular assemblies that may result in hydrogelation inside HeLa cells.

We also incubated the HeLa cells with **1a** (500 μM) at 4 or 37 °C for 20 h and determined the concentration of **1a** and **1b** inside the cells (Table S1). As the result shows in Figure 2A, at 4 °C, the concentrations of **1a** and **1b** are 1.49−5.37 mg/mL (1.75−6.29 mM) and 0.99−3.55 mg/mL (1.28−4.57 mM), respectively. In addition, **1b** forms a hydrogel at 1.8 mg/mL (2.35 mM) even if it is generated enzymatically at 4 °C (Figure S3C). At 37 °C, the concentration of **1b** is 0.13−0.46 mg/mL (0.17−0.60 mM), while **1a** is undetectable, similar to the 48 h incubation at the same temperature. These results have three major implications: first, the presence of **1a** in addition to **1b** inside cells incubated at 4 °C suggests that the precursor of **1a** enters the cells *via* energy-independent processes, such as passive diffusion,[35] but then its intracellular conversion to mature hydrogelator **1b** and self-assembly to molecular assemblies is incomplete, likely due to greatly reduced enzyme activity at 4 °C. In contrast, at 37 °C virtually all intracellular **1a** has been converted into **1b** after both 20 and 48 h. Second, despite the slower **1a**-to-**1b** conversion and the rate of self-assembly inside the cells incubated at 4 °C, the total concentration of **1b** at 37 °C is considerably lower than at 4 °C. Together with the observation of **1b** in lysosomes and Golgi (*vide infra*), this result suggests that the cells actively reduce the presence of intracellular molecular assemblies in a process that is slowed at low temperatures. Third, there is more **1b** inside the cells after 48 h of incubation than 20 h of incubation at 37 °C, confirming the accumulation of **1b** over time and implying an inefficient removal of the nanofibers by the cells.

Our results show that the precursor molecules can passively diffuse through the membranes, which should also allow them to enter the membrane-enclosed organelles. To determine the distribution of phosphatases in different cell compartments and to infer the possible cellular location of the enzymatic dephosphorylation of **1a** and hydrogelation, we fractioned the cell components using differential centrifugation.[36] After lysing HeLa cells by differential centrifugation, we obtained five cell fractions: **N** (nuclei), **M** (mitochondria, lysosomes, and peroxisomes), **P** (plasma membrane, microsomal fraction (= fragments of endoplasmic reticulum, golgi, and other vesicles), and large polyribsomes),

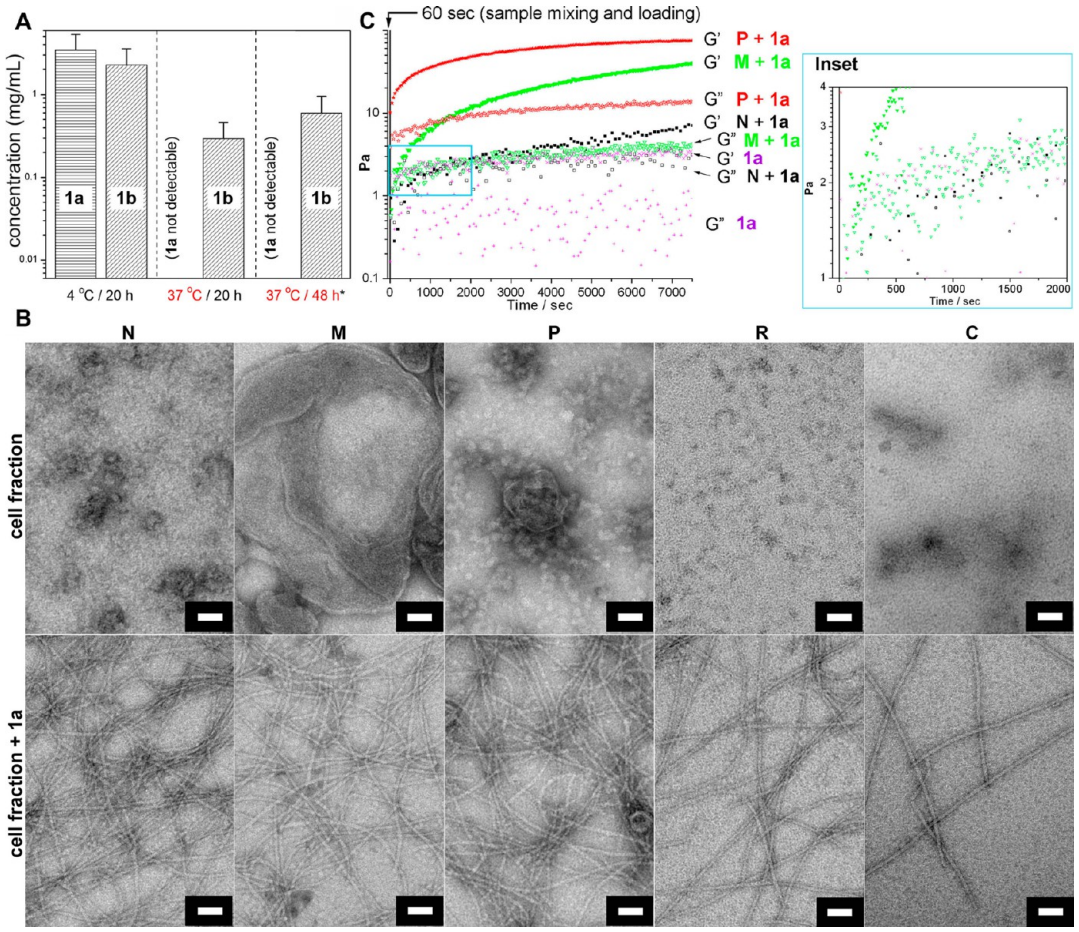

Figure 2. (A) The average intracellular concentrations of precursor 1a and hydrogelator 1b were determined by LC-MS after incubating HeLa cells with precursor 1a at a concentration of 500 μM and temperatures of 4 or 37 °C up to 2 days. (*These cells were co-incubated with additional 2a at the concentration of 200 nM.) (B) Typical TEM images showing the morphology of each cell fraction itself and with the addition of 1a at the concentration of 6 mg/mL after 24 h (for N, M, and P) and 48 h (for R and C). Scale bar: 500 nm for cell fraction N (no 1a) and 50 nm for the rest. (C) Storage/loss modulus measurement at a time mode by oscillatory rheometry showing the gelation points of the mixture of each cell fraction with 1a at a concentration of 6 mg/mL; (Inset) Enlarged area boxed by the blue lines in (C).

R (ribosomal subunits and small polyribosomes), and **C** (cytosol). After fractionation, 100 μL of each fraction is mixed with 200 μL of **1a** (final concentration in the mixture is 6 mg/mL) for estimating the time required for hydrogelation by visual inspection. Fraction **P** induces hydrogelation faster (<2 h) than fraction **N** or **M** does (overnight), while fractions **R** and **C** fail to convert the mixture into a self-supported hydrogel.[15] Negative-staining EM[37] of the cell fractions alone (Figure 2B, top row) and after 24 h incubation with **1a** (Figure 2B, bottom row) confirms the presence of molecular assemblies of **1b** fibers only in latter samples. Although the molecular assemblies in the samples with hydrogelator exhibit identical morphologies (*i.e.*, widths of 10 $\pm$ 2 nm), the density and cross-linking of the molecular assemblies is considerably higher in cell fractions **P**, **N**, and **M** than in **R** and **C** (Figure 2B). Although we observed cell fractions to cause the molecular self-assembly previously, here we use rheometry to determine the gelation point more precisely for the comparison of the capability of triggering hydrogelation by each cell fraction. The storage modulus G' and loss modulus G'' measured in rheological tests confirm that the cross-linking and the density of molecular assemblies are higher inside the samples treated with fractions **P**, **N**, and **M** than those treated with **R** and **C** (Figure S4). To quantify the rate of formation of the molecular assemblies, we used oscillating rheometry to measure the gelation point, *i.e.*, the time point when G' dominates G'',[38] for **1a** mixed with the cell fractions **N**, **M**, and **P**. As shown in Figure 2C, the gelation points for the mixtures are less than 60 s for fraction **P** (which is within the sample mixing and loading time), 1560 s for **N**, and 260 s for **M**. The highest rate of formation of molecular assemblies and hydrogelation in the sample with cell fraction **P** indicates that a large amount of intracellular molecular assemblies should associate with the cellular components of the **P** fraction. We also examined the cell fractions by TEM after incubating the HeLa cells with the precursor (**1a**). We found cell fractions **M** and **P** containing nanofibers (with a width of 10 $\pm$ 2 nm), which are absent in fractions **M** and **P** of untreated HeLa cells

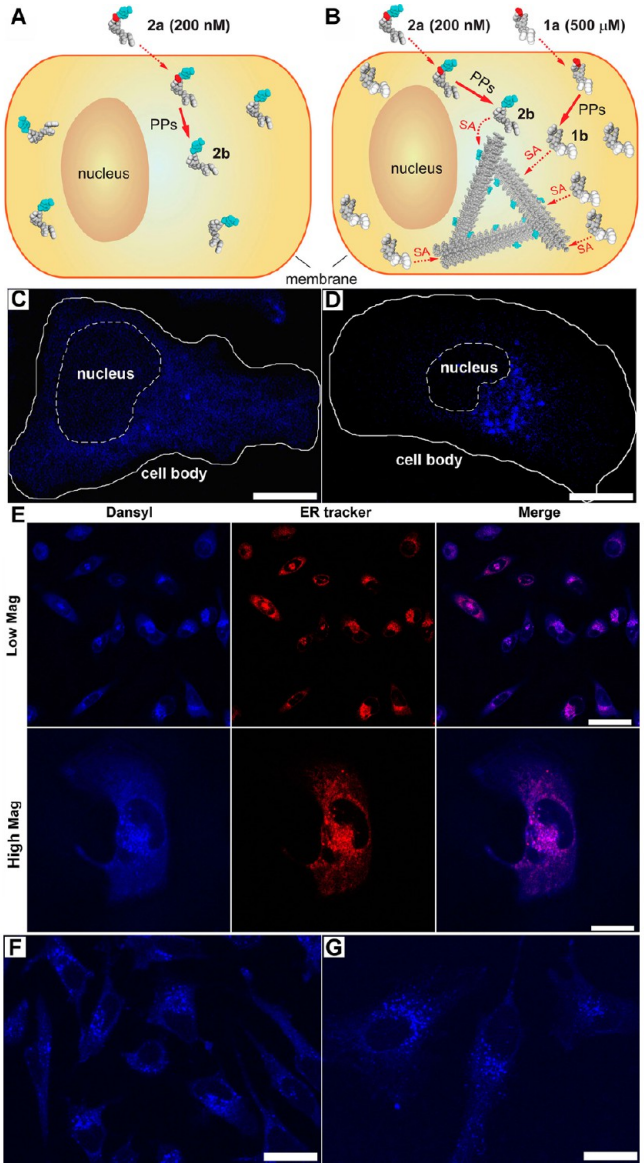

Figure 3. Illustrations (A, B) and fluorescence images (C, D) of two experiments that use a precursor mixture of 1a+2a (B, D) or only 2a (A, C). HeLa cells incubated with precursor 2a alone at 200 nM, which allows fluorescence imaging, but is lower than the critical concentration for filament self-assembly, show weak diffuse fluorescence throughout the cytosol (C), indicating the lack of formation of the molecular assemblies (A). Incubating HeLa cells with a precursor mixture of 200 nM 2a and 500 μM 1a results in intensified fluorescence localized to spots close to the nucleus (D), indicating the formation of 1b/2b molecular assemblies (B). Scale bars: 15 μm (SA = self-assembly, PP = protein phosphatase). (E) Confocal images of HeLa cells incubated under the same conditions as shown in (B) and stained with ER-Tracker. Scale bars: 50 μm (top row); 20 μm (bottom row). Confocal images of the HeLa cells incubated by (F) sequence I or (G) sequence II (see text for details). Scale bars: 25 μm.

(Figure S5). This result supports the formation of molecular assemblies inside the cells. The appearance of the nanofibers in fraction **M** likely arises from the high molecular weight of the nanofiber network to allow them to be more sedimentable.

For the study of the localization of molecular assemblies inside HeLa cells by fluorescent microscopy, we incubated HeLa cells with a mixture of the fluorescent precursor **2a**, at low enough concentration with respect to image quality (photon saturation issue) and cytotoxicity, and the nonfluorescent precursor **1a**, at high enough concentration to induce self-assembly for generating **1b**/**2b** molecular assemblies. Hydrogelators **1b** and **2b** share the same self-assembly motif, which allows the mixture of **1b** and **2b** to form molecular assemblies at the critical concentration of **1b** (235 μM, Figure S1). This method provides a simple way to permit using fluorescence imaging to determine subcellular localization of the molecular assemblies inside cells (Figure 3).

After incubating the HeLa cells with precursor **2a** alone at a subcritical concentration (200 nM) for 48 h or above the critical concentration with **1a** (500 μM) and **2a** (200 nM) together, the cells were washed by an additional incubation (24 h) in precursor-free culture medium to remove any extracellular **2a** and to reduce

the background. Confocal imaging of these HeLa cells (Figure 3C and D, Figure S6A,B) reveals several features: (i) the nucleus and the cell surface show little fluorescence (further confirmed in Figure S7A), suggesting that the fluorescent molecules (**2a**, **2b**, and **1b**/**2b** molecular assemblies) neither attach to the cell surface nor enter the nucleus. (ii) At subcritical concentration of the precursor **2a** (200 nM), **2b** distributes almost uniformly in the cytosol (Figure 3C), indicating little specific binding between individual molecules of **2b** and specific cellular organelles. (iii) Above the critical concentration of **1a** (500 μM) mixed with **2a** (200 nM), the fluorescence is more concentrated, especially in spots that localize near the nucleus, suggesting that the **1b**/**2b** molecular assemblies localize at the region of the endoplasmic reticulum (further confirmed in Figure 3E) and/or Golgi.

We used ER-Tracker Red dye to stain the cells after the above-described incubation with **1a** and **2a** to confirm co-localization of the **1b**/**2b** molecular assemblies with the ER region. Figure 3E shows that the blue fluorescence from the dansyl group overlaps completely with the red fluorescence from the ER-Tracker, confirming that the molecular assemblies made of **1b** and **2b** localize to the ER. In contrast, there is little overlap between the signal of **1b**/**2b** molecular assemblies and the orange fluorescence of the nucleic acid stain, SYTO 85 (Figure S7 A), confirming that the molecular assemblies are unlikely to localize in the nuclei or mitochondria. We also used Golgi tracker (BODIPY TR C_5-ceramide complexed to BSA) and LysoTracker Red DND-99 to stain Golgi and lysosomes and found that the fluorescence of molecular assemblies partially overlaps with both organelles (Figure S7B,C), suggesting that cells likely process the molecular assemblies *via* the secretion pathway (ER−Golgi−lysosomes/secretion).

To confirm both that **1b** and **2b** coassemble into **1b**/**2b** molecular assemblies and that **2b** integrates into preassembled **1b** molecular assemblies inside the cells, we changed the order of the addition of **1a** and **2a** to the HeLa cells. Sequence I is to add **2a** (200 nM) at day 1, wash with the buffer solution at day 2, and add **1a** (500 μM) at day 3; in contrast, sequence II is to add **1a** (500 μM) at day 1, add **2a** (200 nM) at day 2, and wash with the buffer at day 3. As shown in Figure 3, the localization of **2b** to the ER region occurs with both sequence I (Figure 3F) and sequence II (Figure 3G). Both experiments result in similar images to that shown in Figure 3D, indicating that the intracellular molecular assemblies recruit other small molecules with the same self-assembly motif for the integration into the nanofibers. Additionally, the cell viability assays indicate little cytotoxicity of **1a** and **2a** at concentrations lower than 500 μM[33] and 200 μM (data not shown here), respectively. Therefore, the localization of the molecular assemblies is unlikely a result of the cells undergoing cell death.

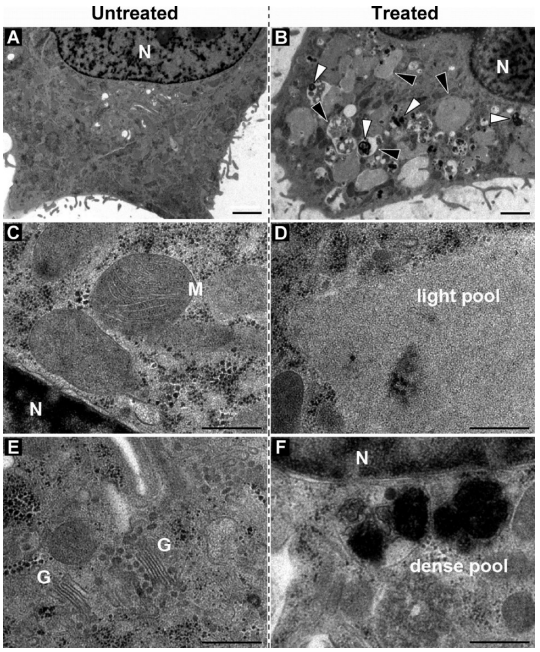

Figure 4. TEM images of the high-pressure frozen/freeze-substituted and plastic-sectioned HeLa cells that were either untreated (A) or incubated with 500 μM precursor 1a (B). Note the pools of low electron-dense (black arrowheads) and electron-dense material (white arrowheads) in the treated cells. (C−F) The same as in the top row, but the ultrastructure is shown at higher magnification. N, nucleus; M, mitochondria; G, golgi stack. Scale bars: 2 μm (top), 500 nm (C−F).

We also used transmission electron microscopy (TEM) of high-pressure frozen/freeze-substituted HeLa cells to study the effects of the molecular assemblies on the cellular ultrastructure. The structural comparison of the untreated HeLa cells (as the control, Figure 4A) with the HeLa cells treated with 500 μM precursor **1a** reveals several modifications and a few new structural features (Figure 4B). At a higher magnification, Figure 4D and F show two types of membrane-bound compartments: the large pools of the materials with low electron density and the smaller vesicles with highly electron-dense substances. While the light compartments could be the large vesicles derived from the ER that include the accumulated hydrogelators, the darker granules could be the lysosomes with the molecular assemblies that appear to undergo degradation (evidenced by the observation of the fragment of **1a** in LC-MS analysis (Figure S3A,B). This result suggests that the HeLa cells likely treat the molecular assemblies of **1a** as proteins targeted for degradation. To verify if the membrane-bound compartments associate with autophagy, we incubated the HeLa cells with **1a** and rapamycin, an antibiotic that induces autophagy, to reduce the toxicity of abberant proteins.[39] We found that rapamycin hardly decreased the cytotoxicity of **1a**, which suggested that the degradation of **1a** or **1b** *via* autophagy is unlikely.

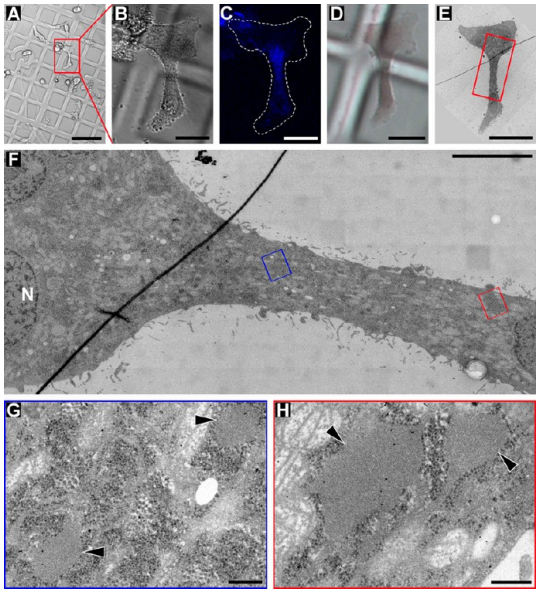

Figure 5. Correlative light and electron microscopy (CLEM) of HeLa cells incubated for 48 h with 500 μM 1a and 200 nM 2a. (A–C) DIC and fluorescence light microscopy images of treated HeLa cells growing on Aclar plastic film; the low-magnification DIC overview (A), the zoom-in DIC image (B) of one cell of interest (red box in A), and the zoom-in fluorescence image (B) of the same cell were recorded only a few minutes before the sample was high-pressure frozen; note that the Aclar film was marked with a pattern for tracking cells of interest throughout the CLEM sample preparation. In (C) note the highest intensity of fluorescence signal in the narrow part of the cell, indicating a high abundance of hydrogelator in that region of the cell. (D) DIC light microscopy image of the same cell of interest shown in (B) and (C), but after high-pressure freezing, freeze-substitution, and resin-embedding; note that the Aclar pattern is still visible to guide trimming of the resin block before cutting ultrathin plastic sections (70 nm thick) that can be inspected in the transmission electron microscope. (E) Low-magnification TEM image of the cell of interest shown in (B)–(D). (F) Higher magnification electron micrograph of the neck region (red box in E) of the same cell shown in (B)–(E); the narrow neck region of the cell corresponds to the area of highest fluorescence signal (in C); the image displays a large specimen area at relatively high resolution, because it is a "montage image" that was stitched together from 220 individual high-magnification image tiles. (G, H) High-magnification electron micrographs of the (G) blue boxed area and (H) the red boxed area in (F); note the presence of low electron-dense pools (black arrowheads), presumably containing hydrogelator. Scale bars: 100 μm (A), 25 μm (B, C, D, E), 5 μm (F), and 250 nm (G, H).

To demonstrate that the observed ultrastructural changes of the treated cells (Figure 4) are directly connected to the self-assembly of the molecular assemblies of **1b**, we used CLEM to image the HeLa cells treated with **1a** and **2a**. This allows us to correlate the fluorescence signal of **1b**/**2b** molecular assemblies imaged in live cells just before their rapid freezing for the EM sample preparation. The ultrastructural organization of the same cells was imaged by TEM (Figure 5). CLEM reveals a high accumulation of vesicles with low electron-dense material in the cytoplasmic region that also shows high fluorescence signal. Moreover, the CLEM experiment on a healthy cell (which adheres and spreads on the grid) establishes the direct correlation between the fluorescent region and the features observed in TEM, which excludes the possibility that the features in TEM arise from cellular stresses that would affect the entire lumen. Although the filamentous assemblies and the bundles are observed in the cytoplasm of the treated (and untreated) HeLa cells, the resolution of the plastic section TEM is not sufficient to unambiguously distinguish molecular assemblies from endogenous cytoskeletal intermediate or actin filaments. Molecular assembly specific electron-dense labels are not available. Therefore further studies are required for a detailed description of the micromorphology of intracellular molecular assemblies, to verify whether the low electron density material in the vesicles is a hydrogel-forming network of molecular nanofibers (Figure S8A). A modified method for EM sample preparation may be desired since the solvent displacement during EM sample preparation here could somehow blur the nanostructure of molecular assemblies, which makes the fine structure indistinguishable (Figure S8B).

Several facts help exclude the possibility that cellular segregation alone results in the agglomeration in the cells. First, the CLEM study reveals not only that the fluorescent molecular agglomerations are adjacent to each other but also that the fluorescent area superimposes with the molecular agglomeration shown in TEM. Second, if the agglomeration is induced by cellular segregation, these resulting vesicles should widely spread within the cytoplasm. But they localize in a confined area to indicate that the agglomeration is unlikely induced by cellular segregation. Third, we designed and synthesized a third molecule, **3a** (Figure S9), which has a very similar structure to **1a** and **2a**. Specifically, **3a** consists of a rhodamine group *via* the ε-lysine linkage. In a gelation test, we find that the solution of **3a** fails to form a hydrogel after dephosphorylation (Figure S10), indicating that **3a** is unable to form nanofibers before and after dephosphorylation. When we incubate HeLa cells with **3a** at a concentration of 500 μM, the cells are homogeneously shown in red instead of producing any agglomeration within the cytoplasm (Figure S11). This result further supports that enzyme-instructed self-assembly results in the localization of the agglomeration of the hydrogelator of **1b**.

CONCLUSIONS

In conclusion, the molecular assemblies of self-assembled small molecules behave drastically different from the individual molecules. The reported model system not only allows intracellular formation of nanostructures *via* enzyme-instructed molecular self-assembly but also offers a new way for elucidating and utilizing the emerging properties of supramolecular

assemblies of small molecules inside cells. For example, intracellular formation of molecular assemblies could be used selectively to inhibit the growth of cells that overexpress certain enzymes.[6,7,40] The further development of molecular self-assembly-based[41−43] approaches for understanding and modulating fundamental cellular process (*e.g.*, proteostasis[44]) and for exploring its potential applications in biomedicine (*e.g.*, intracellular drug delivery[45]) may ultimately lead to a new way to regulate cellular functions. The small size of the precursors and the simplicity of the enzyme-instructed self-assembly process should also facilitate the delineation of the molecular details of the molecular assemblies from the complex cellular process.

MATERIALS AND METHODS

A. Materials. Alkaline phosphatase (ALP) was purchased from Biomatik USA, LLC, dansyl chloride (DNS-Cl) was from Sigma-Aldrich, 2-naphthylacetic acid and *N*-hydroxysuccinimide were from Alfa Aesar, *N*,*N*′-dicyclohexylcarbodimide was from Acros Organics USA, all amino acid derivatives were from GL Biochem (Shanghai) Ltd., and ER-Tracker Red (glibenclamide BODIPY TR) and SYTO 85 orange fluorescent nucleic acid stain were from Invitrogen and used according to the protocols.

B. Instruments. Fluorescence spectra were obtained on a Shimadzu RF-5301-PC fluorescence spectrophotometer; LC-MS on a Waters Acquity Ultra Performance LC with a Waters Micromass detector and rheological tests on ARES-G2 rheometer. Electron microscopy was performed on a FEI Morgagni 268 TEM with a 1k CCD camera (GATAN, Inc., Pleasanton, CA, USA) or a 300 keV Tecnai F30 intermediate voltage TEM (FEI, Inc., Hillsboro, OR, USA) with a 4k CCD camera (GATAN). Confocal images were obtained with a Leica TCS SP2 spectral confocal microscope. The MTT assay for cell toxicity testing was performed on a DTX880 multimode detector.

C. General Methods. Briefly, the *in vitro* hydrogelation test was monitored with the addition of ALP into each hydrogelator precursor solution. The resulting fibril structures were identified by TEM with a general negative staining method. The concentrations of each compound inside the cells were determined according to the integration of the corresponding peak from the LC-MS trace of the lysate of cells incubated at various conditions. For all confocal images, the cells were seeded on a Lab-Tek II chambered coverglass and treated with conditions as described in the main text.

D. Cell Fragmentation (ref 27). 600*g*, 10 min: pellet sample **N** (nuclei); 15000*g* 5 min: pellet sample **M** (mitochondria, lysosomes, peroxisomes); 100000*g*, 60 min: pellet sample **P** (plasma membrane, microsomal fraction (fragments of endoplasmic reticulum), large polyribsomes); 300000*g*, 120 min: pellet sample **R** (ribosomal subunits, small polyribosomes); supernatant sample **C**: soluble portion of cytoplasm (cytosol).

Pellets **N**, **M**, **P**, and **R** were all redispersed in 200 μL of PBS for further testing.

E. Sample Preparation and Electron Microscopy of Cells. Aclar discs with a 1.5 mm diameter were punched out of Aclar film (EMS, #50426-10; Fort Washington, PA, USA) and mounted on a Lab-Tek II chambered coverglass (#155379 Nalge Nunc International). HeLa cells were then seeded on the coverglass including the Aclar discs and grown to less than confluent density in minimum essential medium and 10% FBS (Invitrogen). Cells treated with the hydrogelator were incubated with the precursor for 48 h before light microscopy and EM preparation. Cells were imaged by phase contrast and/or fluorescent light microscopy using an inverted Leica SP2 confocal laser scanning microscope. After light microscopic imaging, the Aclar discs with the cells were transferred into half of an aluminum planchette (Wohlwend, Switzerland) covered with a drop of medium containing 150 mM sucrose as cryoprotectant for high-pressure freezing, and the second half of the planchette was added to enclose the cells in a cavity with a 0.1 mm height. The samples were rapidly frozen using a Leica HPM-100 high-pressure freezer (Leica Microsystem, Vienna, Austria). The frozen cells were freeze-substituted at low temperatures over 3 days in a solution containing 1% osmium tetroxide (EMS), 0.5% anhydrous glutaraldehyde (EMS), and 2% water in anhydrous acetone (AC32680-0010 Fisher Scientific) using a Leica AFS-2 device. After the temperature was raised to 4 °C the cells were infiltrated and embedded in EMbed 812-Resin (EMS). Ultrathin sections (~70 nm) were collected on slot grids covered with Formvar support film and poststained with uranyl acetate (supersaturated solution) and 0.2% lead citrate, before being inspected using a FEI Morgagni 268 TEM with a 1k CCD camera (GATAN) or a 300 keV Tecnai F30 intermediate voltage TEM (FEI) with a 4k CCD camera (GATAN). For large overviews of the cells at medium magnification we acquired montages of overlapping images in an automated fashion using the microscope control software SerialEM.[46]

For CLEM, we grew cells on Aclar discs that were marked with a pattern that allowed tracking of cells of interest throughout the light microscopy and EM sample preparation. After locating cells of interest, *e.g.*, those containing fluorescently labeled hydrogelator, by light microscopy, the cells were rapidly frozen, fixed, and resin-embedded as described above. For TEM analysis, the block was trimmed, guided by the pattern on the Aclar disc, so that only the quadrant containing the cells of interest remained for ultrathin sectioning. After poststaining of the sections, we recorded overview maps of the sections at low magnification in the TEM to localize again the cell(s) of interest, before recording images at higher magnification for the ultrastructural investigation.

Conflict of Interest: The authors declare no competing financial interest.

Supporting Information Available: TEM images, LC-MS, rheology, fluorescent images, and procedures for cell fractionation and EM sample preparation. This material is available free of charge *via* the Internet at http://pubs.acs.org.

Acknowledgment. This work was partially supported by NSF (DMR 0820492) to B.X. and D.N., by an HFSP grant (RGP0056/2008) and an NIH grant (R01CA142746) to B.X., by start-up funds from Brandeis University, and by NSF (MRI NSF 0722582) to D.N. Light and electron microscopy was performed at the Brandeis imaging facilities. We thank Mr. Wenbo Pei for help on LC-MS experiments.

REFERENCES AND NOTES

1. Fletcher, D. A.; Mullins, D. Cell Mechanics and the Cytoskeleton. *Nature* **2008**, *463*, 485–492.
2. Spillantini, M. G.; Crowther, R. A.; Jakes, R.; Hasegawa, M.; Goedert, M. Alpha-Synuclein in Filamentous Inclusions of Lewy Bodies From Parkinson's Disease and Dementia with Lewy Bodies. *Proc. Natl. Acad. Sci. U.S.A.* **1998**, *95*, 6469–6473.
3. Pollard, T. D.; Cooper, J. A. Actin, a Central Player in Cell Shape and Movement. *Science* **2009**, *326*, 1208–1212.
4. Perng, M. D.; Cairns, L.; van den Ijssel, P.; Prescott, A.; Hutcheson, A. M.; Quinlan, R. A. Intermediate Filament Interactions Can Be Altered by HSP27 and Alpha B-Crystallin. *J. Cell Sci.* **1999**, *112*, 2099–2112.
5. Rubinsztein, D. C. The Roles of Intracellular Protein-Degradation Pathways in Neurodegeneration. *Nature* **2006**, *443*, 780–786.
6. Yang, Z.; Liang, G.; Guo, Z.; Xu, B. Intracellular Hydrogelation of Small Molecules Inhibits Bacterial Growth. *Angew. Chem., Int. Ed.* **2007**, *46*, 8216–8219.

7. Yang, Z. M.; Xu, K. M.; Guo, Z. F.; Guo, Z. H.; Xu, B. Intracellular Enzymatic Formation of Nanofibers Results in Hydrogelation and Regulated Cell Death. *Adv. Mater.* **2007**, *19*, 3152–3156.
8. Estroff, L. A.; Hamilton, A. D. Water Gelation by Small Organic Molecules. *Chem. Rev.* **2004**, *104*, 1201–1217.
9. Terech, P.; Weiss, R. G. Low Molecular Mass Gelators of Organic Liquids and the Properties of Their Gels. *Chem. Rev.* **1997**, *97*, 3133–3159.
10. Ulijn, R. V.; Smith, A. M. Designing Peptide Based Nanomaterials. *Chem. Soc. Rev.* **2008**, *37*, 664–675.
11. Fischer, P. M.; Krausz, E.; Lane, D. P. Cellular Delivery of Impermeable Effector Molecules in the Form of Conjugates with Peptides Capable of Mediating Membrane Translocation. *Bioconjugate Chem.* **2001**, *12*, 825–841.
12. Zorn, J. A.; Wille, H.; Wolan, D. W.; Wells, J. A. Self-Assembling Small Molecules Form Nanofibers That Bind Procaspase-3 to Promote Activation. *J. Am. Chem. Soc.* **2011**, *133*, 19630–19633.
13. Kuang, Y.; Xu, B. Disruption of the Dynamics of Microtubules and Selective Inhibition of Glioblastoma Cells by Nanofibers of Small Hydrophobic Molecules. *Angew. Chem., Int. Ed.* **2013**, *52*, 6944–6948.
14. Kumar, R. K.; Yu, X. X.; Patil, A.; Li, M.; Mann, S. Cytoskeletal-like Supramolecular Assembly and Nanoparticle-Based Motors in a Model Protocell. *Angew. Chem., Int. Ed.* **2011**, *50*, 9343–9347.
15. Gao, Y.; Shi, J. F.; Yuan, D.; Xu, B. Imaging Enzyme-Triggered Self-Assembly of Small Molecules Inside Live Cells. *Nat. Commun.* **2012**, *3*, 1033.
16. Sameiro, M.; Goncalves, T. Fluorescent Labeling of Biomolecules with Organic Probes. *Chem. Rev.* **2009**, *109*, 190–212.
17. Zimmer, M. Green Fluorescent Protein (GFP): Applications, Structure, and Related Photophysical Behavior. *Chem. Rev.* **2002**, *102*, 759–781.
18. Medintz, I. L.; Uyeda, H. T.; Goldman, E. R.; Mattoussi, H. Quantum Dot Bioconjugates for Imaging, Labelling and Sensing. *Nat. Mater.* **2005**, *4*, 435–446.
19. Resch-Genger, U.; Grabolle, M.; Cavaliere-Jaricot, S.; Nitschke, R.; Nann, T. Quantum Dots *versus* Organic Dyes as Fluorescent Labels. *Nat. Methods* **2008**, *5*, 763–775.
20. Wang, K.; Rodgers, M. E.; Toptygin, D.; Munsen, V. A.; Brand, L. Fluorescence Study of the Multiple Binding Equilibria of the Galactose Repressor. *Biochemistry* **1998**, *37*, 41–50.
21. Taniguchi, Y.; Choi, P. J.; Li, G. W.; Chen, H. Y.; Babu, M.; Hearn, J.; Emili, A.; Xie, X. S. Quantifying E-coli Proteome and Transcriptome with Single-Molecule Sensitivity in Single Cells. *Science* **2010**, *329*, 533–538.
22. Freudiger, C. W.; Min, W.; Saar, B. G.; Lu, S.; Holtom, G. R.; He, C. W.; Tsai, J. C.; Kang, J. X.; Xie, X. S. Label-Free Biomedical Imaging with High Sensitivity by Stimulated Raman Scattering Microscopy. *Science* **2008**, *322*, 1857–1861.
23. Channon, K. J.; Devlin, G. L.; MacPhee, C. E. Efficient Energy Transfer within Self-Assembling Peptide Fibers: A Route to Light-Harvesting Nanomaterials. *J. Am. Chem. Soc.* **2009**, *131*, 12520–12521.
24. Chen, L.; Revel, S.; Morris, K.; Adams, D. J. Energy Transfer in Self-Assembled Dipeptide Hydrogels. *Chem. Commun.* **2010**, *46*, 4267–4269.
25. Yang, Z.; Liang, G.; Xu, B. Enzymatic Hydrogelation of Small Molecules. *Acc. Chem. Res.* **2008**, *41*, 315–326.
26. Li, J. Y.; Gao, Y.; Kuang, Y.; Shi, J. F.; Du, X. W.; Zhou, J.; Wang, H. M.; Yang, Z. M.; Xu, B. Dephosphorylation of D-Peptide Derivatives to Form Biofunctional, Supramolecular Nanofibers/Hydrogels and Their Potential Applications for Intracellular Imaging and Intratumoral Chemotherapy. *J. Am. Chem. Soc.* **2013**, *135*, 9907–9914.
27. Li, J. Y.; Kuang, Y.; Gao, Y.; Du, X. W.; Shi, J. F.; Xu, B. D-Amino Acids Boost the Selectivity and Confer Supramolecular Hydrogels of a Nonsteroidal Anti-Inflammatory Drug (NSAID). *J. Am. Chem. Soc.* **2013**, *135*, 542–545.
28. Li, J. Y.; Kuang, Y.; Shi, J. F.; Gao, Y.; Zhou, J.; Xu, B. The Conjugation of Non-steroidal Anti-inflammatory Drugs (NSAID) to Small Peptides for Generating Multifunctional Supramolecular Nanofibers/Hydrogels. *Beilstein J. Org. Chem.* **2013**, *9*, 908–917.
29. Li, J. Y.; Li, X. M.; Kuang, Y.; Gao, Y.; Du, X. W.; Shi, J. F.; Xu, B. Self-delivery Multifunctional Anti-HIV Hydrogels for Sustained Release. *Adv. Healthc. Mater.* **2013**, DOI: 10.1002/adhm.201300041.
30. Smith, C. Two Microscopes are Better Than One. *Nature* **2012**, *492*, 293–297.
31. Vembar, S. S.; Brodsky, J. L. One Step at a Time: Endoplasmic Reticulum-Associated Degradation. *Nat. Rev. Mol. Cell Biol.* **2008**, *9*, 944–957.
32. Zhang, Y.; Kuang, Y.; Gao, Y.; Xu, B. Versatile Small-Molecule Motifs for Self-Assembly in Water and the Formation of Biofunctional Supramolecular Hydrogels. *Langmuir* **2010**, *27*, 529–537.
33. Gao, Y.; Kuang, Y.; Guo, Z. F.; Guo, Z. H.; Krauss, I. J.; Xu, B. Enzyme-Instructed Molecular Self-Assembly Confers Nanofibers and a Supramolecular Hydrogel of Taxol Derivative. *J. Am. Chem. Soc.* **2009**, *131*, 13576–13577.
34. Alberts, B.; Johnson, A.; Lewis, J.; Raff, M.; Roberts, K.; Walter, P. *Molecular Biology of the Cell*, 4th ed.; Garland Science: New York, 2002.
35. Mendez, A. J. Cholesterol Efflux Mediated by Apolipoproteins is an Active Cellular Process Distinct from Efflux Mediated by Passive Diffusion. *J. Lipid Res.* **1997**, *38*, 1807–1821.
36. Dopp, E.; von Recklinghausen, U.; Hartmann, L. M.; Stueckradt, I.; Pollok, I.; Rabieh, S.; Hao, L.; Nussler, A.; Katier, C.; Hirner, A. V.; *et al.* Subcellular Distribution of Inorganic and Methylated Arsenic Compounds in Human Urothelial Cells and Human Hepatocytes. *Drug Metab. Dispos.* **2008**, *36*, 971–979.
37. Frado, L. L.; Craig, R. Electron-Microscopy of the Actin-Myosin Head Complex in the Presence of ATP. *J. Mol. Biol.* **1992**, *223*, 391–397.
38. Nowak, A. P.; Breedveld, V.; Pakstis, L.; Ozbas, B.; Pine, D. J.; Pochan, D.; Deming, T. J. Rapidly Recovering Hydrogel Scaffolds from Self-Assembling Diblock Copolypeptide Amphiphiles. *Nature* **2002**, *417*, 424–428.
39. Levine, B.; Kroemer, G. Autophagy in the Pathogenesis of Disease. *Cell* **2008**, *132*, 27–42.
40. Liang, G. L.; Ren, H. J.; Rao, J. H. A Biocompatible Condensation Reaction for Controlled Assembly of Nanostructures in Living Cells. *Nat. Chem.* **2009**, *2*, 54–60.
41. Huc, I.; Lehn, J. M. Virtual Combinatorial Libraries: Dynamic Generation of Molecular and Supramolecular Diversity by Self-Assembly. *Proc. Natl. Acad. Sci. U.S.A.* **1997**, *94*, 2106–2110.
42. Lehn, J. M. Perspectives in Supramolecular Chemistry-from Molecular Recognition towards Molecular Information-Processing and Self-Organization. *Angew. Chem., Int. Ed.* **1990**, *29*, 1304–1319.
43. Whitesides, G. M.; Mathias, J. P.; Seto, C. T. Molecular Self-Assembly and Nanochemistry-A Chemical Strategy for the Synthesis of Nanostructures. *Science* **1991**, *254*, 1312–1319.
44. Balch, W. E.; Morimoto, R. I.; Dillin, A.; Kelly, J. W. Adapting proteostasis for disease intervention. *Science* **2008**, *319*, 916–919.
45. Lee, Y.; Ishii, T.; Kim, H. J.; Nishiyama, N.; Hayakawa, Y.; Itaka, K.; Kataoka, K. Efficient Delivery of Bioactive Antibodies into the Cytoplasm of Living Cells by Charge-Conversional Polyion Complex Micelles. *Angew. Chem., Int. Ed.* **2010**, *49*, 2552–2555.
46. Mastronarde, D. N. Automated Electron Microscope Tomography Using Robust Prediction of Specimen Movements. *J. Struct. Biol.* **2005**, *152*, 36–51.